INTERFACE

royalsocietypublishing.org/journal/rsif

Research

Cite this article: Schreder HE, Liu J, Kelley DH, Thomas JH, Boster KAS. 2022 A hydraulic resistance model for interstitial fluid flow in the brain. *J. R. Soc. Interface* **19**: 20210812. https://doi.org/10.1098/rsif.2021.0812

Received: 20 October 2021
Accepted: 21 December 2021

Subject Category:
Life Sciences–Engineering interface

Subject Areas:
biomechanics, biomedical engineering, chemical engineering

Keywords:
glymphatic system, interstitial fluid, parenchma

Author for correspondence:
Kimberly A. S. Boster
e-mail: kboster@ur.rochester.edu

Electronic supplementary material is available online at https://doi.org/10.6084/m9.figshare.c.5806753.

THE ROYAL SOCIETY PUBLISHING

A hydraulic resistance model for interstitial fluid flow in the brain

Helena E. Schreder, Jia Liu, Douglas H. Kelley, John H. Thomas and Kimberly A. S. Boster

Department of Mechanical Engineering, University of Rochester, Rochester, NY 14627, USA

DHK, 0000-0001-9658-2954; JHT, 0000-0002-7127-8654; KASB, 0000-0001-5178-128X

Metabolic wastes may be cleared from the brain by the flow of interstitial fluid (ISF) through extracellular spaces in the parenchyma, as proposed in the glymphatic model. Owing to the difficulty of obtaining experimental measurements, fluid-dynamic models are employed to better understand parenchymal flow. Here we use an analytical solution for Darcy flow in a porous medium with line sources (representing penetrating arterioles) and line sinks (representing ascending venules) to model the flow and calculate the hydraulic resistance as a function of parenchymal permeability and ISF viscosity for various arrangements of the vessels. We calculate how the resistance varies with experimentally determined arrangements of arterioles and venules in mouse and primate brains. Based on experimental measurements of the relative numbers of arterioles and venules and their spacing, we propose idealized configurations for mouse and primate brains, consisting of regularly repeating patterns of arterioles and venules with even spacing. We explore how the number of vessels, vessel density, arteriole-to-venule ratio, and arteriole and venule distribution affect the hydraulic resistance. Quantifying how the geometry affects the resistance of brain parenchyma could help future modelling efforts characterize and predict brain waste clearance, with relevance to diseases such as Alzheimer's and Parkinson's.

1. Introduction

Increasing evidence supports the idea that a 'glymphatic system' in the brain functions similarly to the lymphatic system in peripheral tissue, clearing waste and distributing nutrients via fluid transport. Abnormal function of this system has been linked to disorders including hypertension, atherosclerosis, stroke and Alzheimer's disease [1–4]. However, much remains unknown about the glymphatic system, inhibiting the development of interventions that could rehabilitate or compensate for abnormal glymphatic function. Models of fluid flow and solute transport in the glymphatic system can illustrate how its function changes between wakefulness and sleep or between good health and disease [5]. Models can focus and guide experimental efforts by revealing which features of the system are most important to measure accurately. Once validated, a model can be used to predict the effects of various interventions. The usefulness of a model is, of course, limited by its accuracy; therefore, the development of accurate models with appropriate uncertainty bounds is essential. The present study focuses on modelling one important but understudied part of the glymphatic system: the flow from perivascular spaces (PVSs) surrounding penetrating arterioles to the PVSs surrounding ascending venules through the brain parenchyma. The results of this study can be directly incorporated into models of glymphatic flow and transport.

The glymphatic model posits that cerebrospinal fluid enters the brain via PVSs surrounding arterioles and exits the brain via PVSs surrounding venules and/or nerve sheaths [6]. Though PVSs may extend continuously from arterioles to veins via capillaries [7], most studies have focused on the idea that fluid escapes PVSs surrounding arterioles and passes through the extracellular space in brain parenchyma before being taken up at the PVSs around venules [8–14]. Though the

speed of interstitial flow through the parenchyma and the importance of its role in metabolic waste clearance is an open question, increasing evidence supports the idea that interstitial flow may be important for transport of large molecules [9,15]. Some prior works have drawn conclusions about the speed and importance of interstitial flows based on estimates of the hydraulic resistance in the parenchyma. Holter *et al*. [8] modelled parenchymal flow as that from a single line source (arteriole) to a single line sink (venule). Because the parenchyma is punctuated by an array of sources and sinks, the dipole configuration is a simplification that deserves further examination. Ray *et al*. [9] used a computational approach to model flow in three dimensions between rows of evenly spaced arterioles and venules. Real configurations of arterioles and venules do not have even spacing, and therefore a study of the impact of uneven spacing on the predicted flow would be instructive. Vinje *et al*. [10] used a computational approach to model two-dimensional parenchymal flow in an array of sources and sinks, the locations of which were based on experimental data obtained in primate brains [16]. Making those simulations comparable to the many measurements made in the mouse cortex requires significant adjustment, however. Beyond brain size and vessel spacing, the vessel ratio also differs: in the primate cortex, there are approximately two sources (penetrating arterioles) for each sink (ascending venule), whereas in the rodent cortex, there is approximately one source for every three sinks. Accurately modelling hydraulic resistance in the parenchyma is central to the question of the role of interstitial flow in clearance of metabolic waste, which have implications for pathological conditions such as Alzheimer's disease.

Here we model parenchymal flow as a two-dimensional flow in a porous medium owing to an array of parallel line sources (representing PVSs around arterioles) and line sinks (representing PVSs around venules), for which there is an analytical solution. We show that realistic arrays of sources and sinks result in considerably different flow patterns, driving pressures and hydraulic resistances than those for a simple dipole configuration. We first examine how the relative spacing, distribution, and vessel ratio impact the resistance of idealized configurations. We then calculate flows and resistances for vessel arrangements measured *ex vivo* in primate and mouse brains. We show how normal physiological variations (inter-species, inter-subject and intra-subject) affect the hydraulic resistance of the parenchyma.

2. Methods

2.1. Analytical solution for the flow

We model the flow of interstitial fluid (ISF) in the parenchyma as a two-dimensional viscous flow in a porous medium from line sources (representing PVSs around penetrating arterioles) to line sinks (representing PVSs around ascending venules). Line sources and sinks provide an appropriate approximation because the spacing between arteriole and venule PVSs is large compared to their diameters (approx. 3.92 times larger for mice and 4.43 times larger for primates). We use Cartesian coordinates with the z-direction parallel to all line sources and sinks, and therefore approximately perpendicular to the surface of the brain cortex. We denote the two-dimensional location of source (or sink) j as (x_j, y_j). The volume flow rate per unit length emanating from source j (or entering sink j) is q_j. Given a collection of sources and sinks, we determine the pressure and (superficial) fluid velocity by solving Darcy's equation and the continuity equation. Details of the analytical solution are given in appendix B.

When fluid flows along a pathway from an inlet to an outlet in a two-dimensional domain, the hydraulic resistance of that pathway is $\Delta p/q$, where Δp is the pressure drop from inlet to outlet and q is the volume flow rate (per unit vessel length). Brain parenchyma contains many arterioles and venules, so if they are all acting as inlets and outlets, a more useful quantity is the average two-dimensional hydraulic resistance:

$$R = \frac{\bar{p}_{\mathrm{art}} - \bar{p}_{\mathrm{ven}}}{q}, \tag{2.1}$$

where $\bar{p}_{\mathrm{art}}$ and $\bar{p}_{\mathrm{ven}}$ are average values of the arteriole and venule PVS pressures, respectively, and q is the total volume flow rate per unit length. Because the solutions given in appendix B treat arteriole and venule PVSs as line sources and sinks of zero diameter, the pressure diverges at each. To compensate, we calculate $\bar{p}_{\mathrm{art}}$ using the pressure at the edge of each arteriole, a distance r_{art} from the centre, then averaging over all arterioles, where r_{art} is the radius of the penetrating arteriole. Likewise, we calculate $\bar{p}_{\mathrm{ven}}$ using the pressure at the edge of each venule, a distance r_{ven} from the centre, then averaging over all venules, where r_{ven} is the radius of the penetrating venule. Changing the angular location of the point on the edge of the vessel where we calculate the pressure changes the resistance by less than 1%. Changing the size of the radius by 10% changes $\mathcal{R}_{\mathrm{art}}$ less than 3% for the mice data or 3.5% for the primate data. If we assume that each arteriole PVS emits fluid at the same rate, then $q_j = q/n_a = q/S_j$, where n_a is the number of arterioles and $S_j = n_a$ if the jth element is an arteriole. Likewise, if we assume each venule PVS receives fluid at the same rate $q_j = -q/n_v = -q/S_j$, where n_v is the number of venules and $S_j = -n_v$ if the jth element is a venule. Using these expressions and the one for pressure from appendix B, q can be cancelled out so that the average two-dimensional hydraulic resistance is no longer a function of the flow rate and becomes

$$R = \frac{\mu}{4\pi\kappa}\sum_{j=1}^{J}\left(\sum_{a=1}^{n_a}\frac{1}{n_a\cdot S_j}\ln\frac{(x_0-x_j)^2+(y_0-y_j)^2}{(x_a+r_{\mathrm{art}}-x_j)^2+(y_a-y_j)^2} - \sum_{v=1}^{n_v}\frac{1}{n_v\cdot S_j}\ln\frac{(x_0-x_j)^2+(y_0-y_j)^2}{(x_v+r_{\mathrm{ven}}-x_j)^2+(y_v-y_j)^2}\right). \tag{2.2}$$

R scales with $1/n_a$ because all of the arterioles are in parallel. In other words, R is an extensive measure of hydraulic resistance, in that it depends on the domain size (or equivalently, n_a). R also depends on the viscosity μ of the flowing fluid and the permeability κ of the porous tissue between arterioles and venules. It is useful to define a dimensionless resistance $\mathcal{R}_{\mathrm{art}}$ that is independent of domain size (intensive) and material properties (μ and κ), determined only by the anatomical arrangement of arterioles and venules:

$$\mathcal{R}_{\mathrm{art}} = Rn_a\frac{\kappa}{\mu}. \tag{2.3}$$

We shall report calculated values of the dimensionless hydraulic resistance $\mathcal{R}_{\mathrm{art}}$ throughout the remainder of this paper.

2.2. Boundary conditions

The solution described above satisfies the boundary condition that velocity goes to zero at infinity. We can instead consider a finite domain whose boundaries either are impenetrable or are locations of zero pressure, and an expression for $\mathcal{R}_{\mathrm{art}}$ is given, for both of those cases, in appendix C. However, setting $p = 0$ at the edge of an arbitrary domain within the brain parenchyma excludes the possibility of brain-wide pressure gradients and is therefore unrealistic. Similarly, asserting that arbitrary boundaries within the parenchyma are impenetrable excludes the possibility of flow there and is unrealistic. Moreover, impenetrable boundary

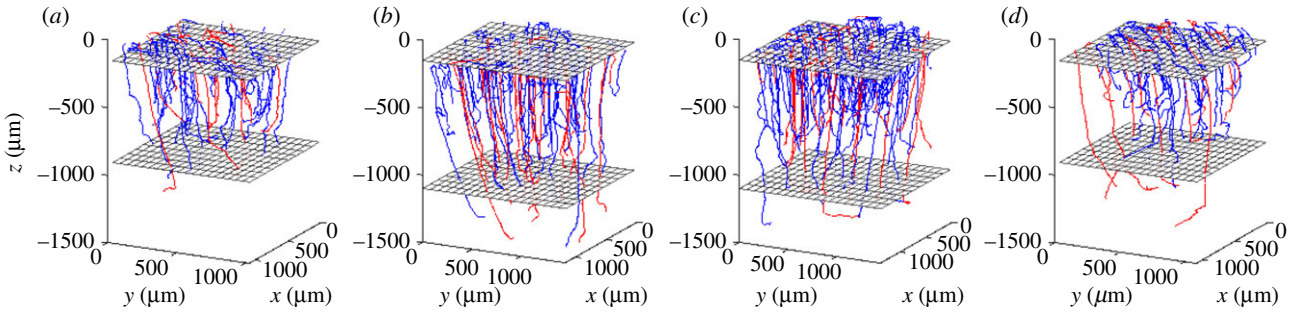

Figure 1. Locations of penetrating arterioles (red) and venules (blue) in the parenchyma of four mice, provided by Blinder *et al.* [17,18] (see appendix A). The gridded cross-sections parallel to the *x*–*y* plane indicate the range of the depths where we use the arteriole and venule locations to model parenchymal flow. We exclude depths of less than 150 μm in order to eliminate pial vasculature. We eliminate depths deeper than the point where the vessel density is less than 20% of its maximum, owing to uncertainty in the imaging. (The exclusion depth for mouse 1 and 4 is 900 μm and for mice 2 and 3 is 1100 μm.)

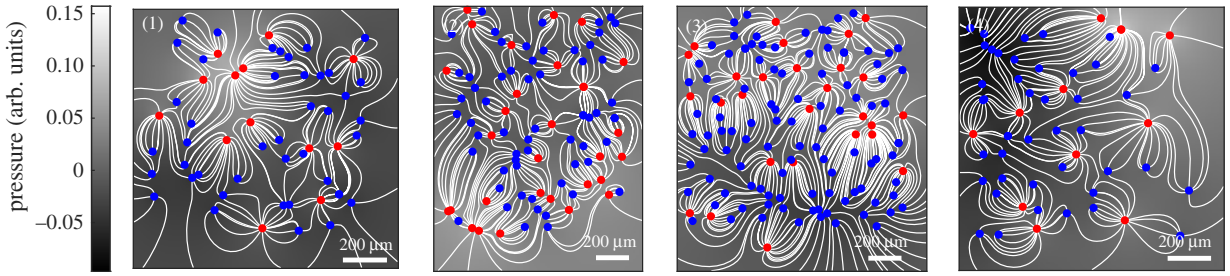

Figure 2. Pressure field and streamlines for an arrangement of arterioles and venules measured in mouse brains [17,18]. Each cross-section is located at a depth of 200 μm into the cortex. Streamlines are represented as white curves, the pressure field is indicated by a grey scale shading, arterioles are in red and venules are in blue. Flow is directed from arterioles (higher pressure) to venules (lower pressure).

conditions tend to impose global pressure gradients inadvertently. Thus, the most physiologically relevant boundary condition is the one in which velocity goes to zero at infinity, and unless otherwise noted, all subsequent discussion will consider that boundary condition. As implied by equation (2.1), hydraulic resistance depends only on pressure differences, so the absolute pressure is irrelevant. That said, we measure all pressures relative to the pressure at an arbitrary point (x_0, y_0), as described in appendix B.

2.3. The arrangement of arterioles and venules

Characterizing parenchymal resistance using equation (2.2) requires specifying the location of each source and sink. We consider arrangements based on *ex vivo* measurements of mouse and primate brains. For the mouse brain, we use $r_{art} = 5.5$ μm and $r_{ven} = 4.5$ μm [17] and the configurations of the penetrating vessels in the vibrissa primary sensory cortex of four mice [17,18], shown in figure 1. The locations where the vessels intersect cross-sections parallel to the cortical surface are obtained as described in appendix A. For the primate brain, we use $r_{art} = 17.8$ μm, $r_{ven} = 23.1$ μm and the configuration shown in fig. 3 of Adams *et al.* [16].

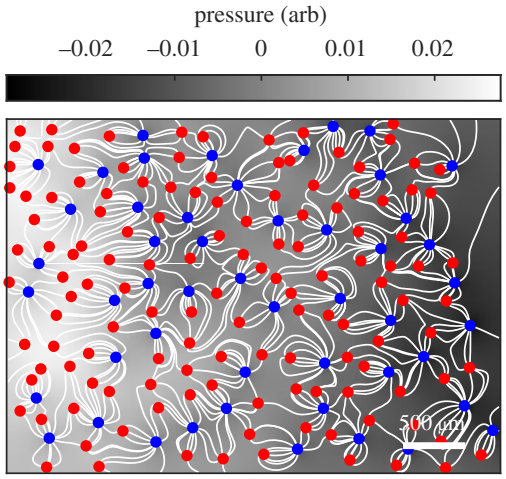

Figure 3. Pressure field and streamlines for an arrangement of arterioles and venules measured in a primate brain [16]. As in figure 2, pressure is represented as a grey scale, streamlines are represented as white curves, arterioles are red and venules are blue. Pressure is higher around clusters of arterioles and lower in regions without arterioles.

3. Results

3.1. *Ex vivo* data

Figure 2 shows examples of the velocity and pressure fields we calculate according to vessel locations in the mouse cortex. The corresponding dimensionless resistances are $\mathcal{R}_{art} = 0.961$, 1.224, 1.090 and 1.165. Figure 3 shows the velocity and pressure fields for an arrangement of arterioles and venules based on data from a primate; the corresponding dimensionless resistance is $R_{art} = 1.669$.

3.2. Idealized arrangements

Having calculated $\mathcal{R}_{art}$ for vessel arrangements measured *ex vivo*, we wondered if parenchymal resistance might be accurately modelled by repeating, simple arrangements of arterioles and venules. Figure 4 shows two such arrangements, accounting for the fact that primates and mice have different vessel ratios. Both arrangements are simpler than *ex vivo* vessel arrangements, starting with the fact that the distance from any vessel to its nearest neighbour is uniform, which reduces the dimensionless resistance. In the primate-like

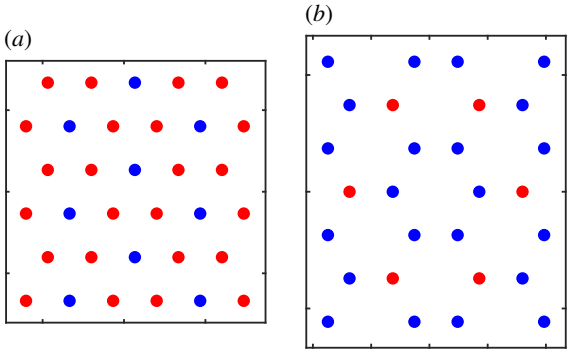

Figure 4. Idealized arrangements for primates (*a*) and mice (*b*). Primates typically have approximately two arterioles for each venule, as in this hexagonal lattice. Mice typically have approximately one arteriole for every three venules, as in this triangular lattice. In both idealized configurations all vessels are equidistant from their nearest neighbours.

arrangement, each venule is surrounded by arterioles, and in the mouse-like arrangement, each arteriole is surrounded by venules. Regular arrangements allow us to quantify how anatomical properties like the number of vessels in the array, vessel density, vessel ratio and vessel arrangement affect the dimensionless resistance.

3.3. Effect of domain size on resistance

The first anatomical property we vary is the number of vessels in the idealized arrangement, or equivalently, the domain size. Figure 5 shows how the dimensionless resistance is affected, with vessel density kept constant, for three different arrangements. In all three, $\mathcal{R}_{art}$ approaches a constant value as the vessel count becomes large. That convergence is consistent with the fact that $\mathcal{R}_{art}$, unlike R, does not scale with n_a (equations (2.2) and (2.3)). We attribute the variation in $\mathcal{R}_{art}$ at small n_a to boundary effects. The converged value of $\mathcal{R}_{art}$ in general depends on the chosen boundary conditions (zero flow at infinity, impermeable boundaries, or zero-pressure boundaries). The converged value varies by 32% among different boundary conditions for the primate data and by 10% for the mouse data. In the special case of a square arrangement, however, $\mathcal{R}_{art}$ converges to the same value (within 1.8×10^{-6}%) for all three boundary conditions. Parenchymal flow has previously been modelled as flow from a single line source to a single line sink [8]. For the boundary condition with zero flow at infinity, this dipole configuration results in a dimensionless resistance $\mathcal{R}_{art}$ that is 28% higher than that for the square arrangement.

If a single value of $\mathcal{R}_{art}$ is to be used when modelling flow in the parenchyma, that value should be determined from a domain size large enough to ensure good convergence. As figure 5 shows, the value of n_a required for convergence depends on both the boundary conditions and the vessel arrangement. Below, we shall assert that the domain is large enough if $\mathcal{R}_{art}$ differs by less than 1% from its value for an array with 10 times as many vessels.

3.4. Effect of vessel density on resistance

The second anatomical property we vary is the vessel density: we change the vessel spacing while holding the aspect ratio of the domain and the vessel ratio constant. $\mathcal{R}_{art}$ decreases with increasing density, as figure 6 shows. The relationship between vessel density and $\mathcal{R}_{art}$ scales similarly for different configurations. We fit the equation

$$\mathcal{R}_{art} = a \ln\left(1 - \frac{b}{\rho^{1/2}}\right), \tag{3.1}$$

to the resistances calculated with equation (2.3), where a and b are fit constants, and ρ is the vessel density (number of vessels per unit area). The form of the fit equation is derived from equation (2.3). The fit captures the relationship between $\mathcal{R}_{art}$ and ρ quite well and shows that $\mathcal{R}_{art}$ scales with density for a regular arrangement of vessels. For the primate idealized configuration, $a = 0.5578$, $b = -2.536 \times 10^4$, and the coefficient of determination is 0.9988; for the mouse idealized configuration $a = 0.2204$, $b = -1.402 \times 10^5$, and the coefficient of determination is 0.9999. The differences in resistance between the idealized mouse configuration the idealized primate configuration arise from differences in the arrangements, including a difference in vessel ratio, as discussed further in the following section, and vessel diameter.

3.5. Effect of vessel ratio on resistance

The third anatomical property we vary is the vessel ratio. Prior models of parenchymal flow have approximated the resistance between even numbers of arterioles and venules [8,9]. However, images of the parenchyma suggest that neither mice nor primates have a 1–1 vessel ratio; primates have a ratio of approximately two arterioles to one venule [16], whereas the ratio for mice is approximately one arteriole to three venules [17]. We explore the effect of the vessel ratio by calculating $\mathcal{R}_{art}$ for idealized arrangements with different vessel ratios in a small unit cell, as shown in figure 7. It is not obvious how to tile each of these arrangements, so we only look at a single cell. Because the domains are small, $\mathcal{R}_{art}$ is not well converged, but its variation among arrangements nonetheless illustrates the dependence on vessel ratio. An array with one arteriole and one venule and inter-vessel spacing of 230 µm has $R_{art} = 0.78$. A triangular array which consists of two arterioles and one venule with the same vessel-to-vessel spacing as the 1–1 ratio has $R_{art} = 1.14$, 46% greater than the 1–1 arrangement. Part of this difference can be explained by the different number of arterioles, since $\mathcal{R}_{art}$ is multiplied by the number of arterioles, but $R\kappa/\mu$ is also different (0.78 in the 1–1 arrangement versus 0.57 in the 2–1 arrangement). We can also compare the resistance for one arteriole and three venules with the same vessel-vessel spacing; in this case $R_{art} = 0.47$, 40% less than the 1–1 ratio. Other configurations with different ratios but the same vessel–vessel spacing (2–2, 3–1, 4–2, 5–2 (A), and 5–2 (B)) all have larger resistances than the 1 : 1 configuration. Clearly, the vessel ratio significantly impacts the hydraulic resistance, and the difference in vessel ratio between species should be considered when modelling parenchymal flow.

Figure 7 also shows that $\mathcal{R}_{art}$ can differ among arrangements with the same vessel ratio. The 2–2 arrangement has the same ratio as the 1–1 arrangement, but the resistance differs: $R_{art} = 0.66$ compared to $R_{art} = 0.78$. Similarly, the 4–2 arrangement has the same ratio as the 2-1 arrangement but different $\mathcal{R}_{art}$ (1.07 compared to 1.14). Arrangements 5-2(A) and 5-2(B) have the same vessel ratio and greater differences in $\mathcal{R}_{art}$ (1.24 compared to 1.78). Arrangement 5.2(B) has

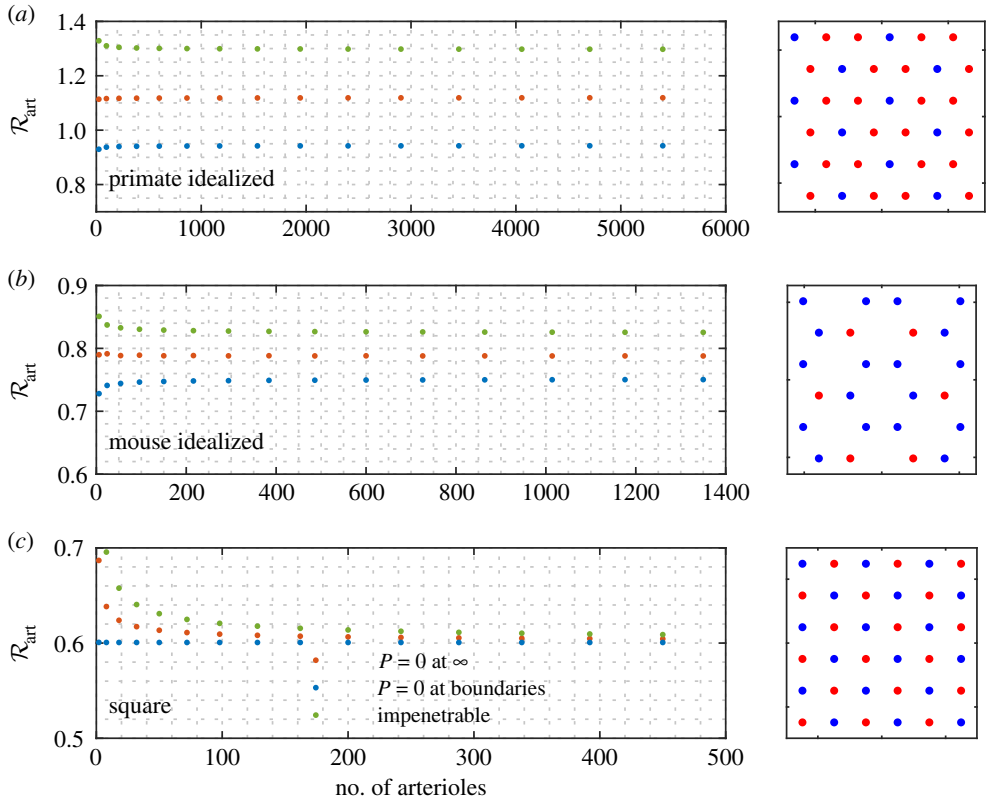

Figure 5. In a repeating arrangement of arterioles and venules, the dimensionless resistance $\mathcal{R}_{art}$ approaches a constant value as the region of interest grows larger, spanning more arterioles. The converged value of $\mathcal{R}_{art}$ and the rate of convergence depend on the boundary condition and the arrangement of vessels, so the appropriate number of vessels needs to be determined independently for each individual case.

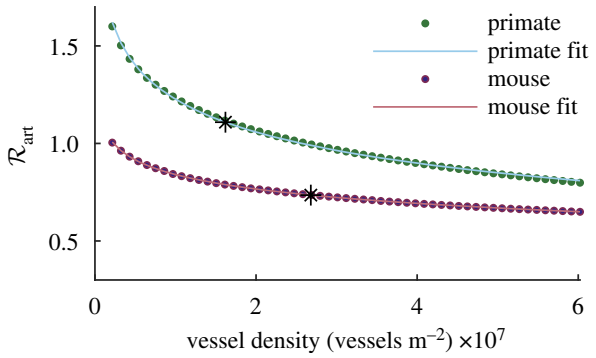

Figure 6. $\mathcal{R}_{art}$ as a function of density for the idealized primate arrangement (*a*) and the idealized mouse arrangement (*b*) shown in figure 4. Markers indicate the $\mathcal{R}_{art}$ calculated with equation (2.3), and the solid curves are equation (3.1) with different fit coefficients for the different idealized arrangements. Equation (3.1) can be used by those modelling parenchymal flow to calculate $\mathcal{R}_{art}$ as a function of density for different species. The non-dimensional resistance $\mathcal{R}_{art}$ differs by a factor of two between the primate and mouse arrangements for the same density, indicating that much of the difference in resistance between the mouse and primate resistances can be attributed to the difference in arrangement, while the rest can be attributed to the difference in average vessel density. Black asterisks indicate the vessel density calculated from in the *ex vivo* primate vessel location data [16] (1.62×10^7 vessels m^{-2}, $\mathcal{R}_{art} = 1.109$) and the average density from the *ex vivo* mouse vessel location data [17,18]) (2.68×10^7 vessels m^{-2}, $\mathcal{R}_{art} = 0.735$)

greater resistance because the typical arteriole-to-venule distance is larger. Generally, $\mathcal{R}_{art}$ depends not only on vessel ratio but also on vessel–vessel distances.

3.6. Effect of vessel arrangement on resistance

Because $\mathcal{R}_{art}$ varies with vessel–vessel distance, and real vessels are not arranged on perfect lattices, it is of interest to examine how $\mathcal{R}_{art}$ would vary if we keep the average vessel–vessel distance unchanged but vary the locations of individual vessels. First, we calculate the resistance of a random arrangement. We place 130 arterioles and 50 venules randomly over a 11.16 µm^2 region; this is approximately the same ratio and exactly the same domain size as the primate data shown in figure 3. (The ratio is 131 to 50 in the primate data.) Figure 8 shows the statistical distribution of resistances for 10 000 different random vessel arrangements (labelled as 'random random'). Placing vessels at random results in a larger $\mathcal{R}_{art}$ than that of the idealized primate arrangement. Because we have primate data for only a single cross section, we cannot construct a statistical distribution, but we can suppose that the arrangement of arterioles and venules is related to the demand for oxygen and therefore more evenly mixed than the random case, leading to a lower resistance. Blinder *et al*. find this to be true in the mouse brain [17].

Next, we consider an arrangement with more structure: we create a hexagonal lattice of 180 vessels and randomly assign vessels as either arterioles or venules ('hex random' in figure 8). This produces a similar $\mathcal{R}_{art}$ distribution to that of the 'random random' arrangement, suggesting that uniform vessel spacing does not make an appreciable difference if vessels are assigned as arterioles or venules randomly. While the spacing between all vessels is uniform, the spacing between arterioles and venules is not uniform; clusters of arterioles or venules can exist, an arrangement unlikely to occur in physiological cases.

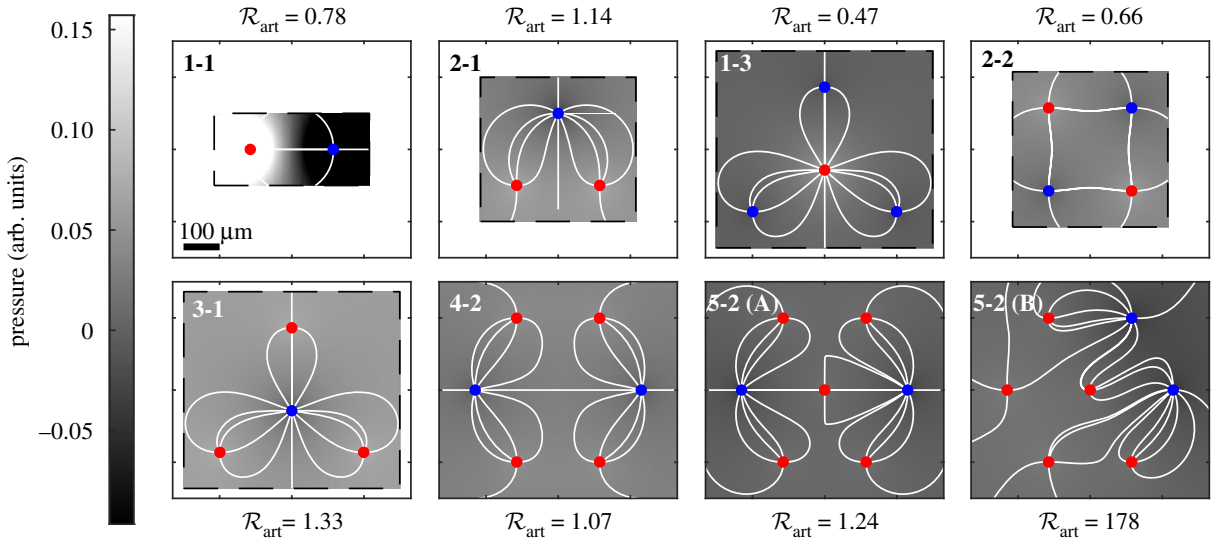

Figure 7. Various arrangements of arterioles (red) and venules (blue) with the same vessel-to-vessel spacing. The resistance is significantly different in each arrangement, showing the impact that the vessel ratio and vessel configuration have on the resistance to flow.

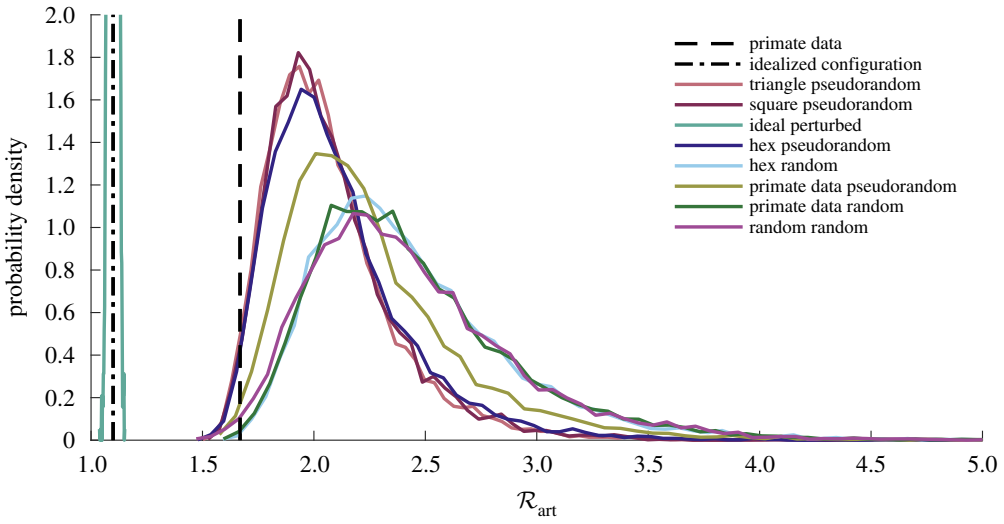

Figure 8. The resistance of various arrangements of vessels with the same density as in the *ex vivo* primate data. The curves show the distribution of resistances obtained from 10 000 different arrangements of arterioles and venules. Physiological or random arrangements of vessels result in higher resistances than the idealized arrangement. Pseudorandom assignments of arterioles and venules result in lower resistances than random assignments.

We also consider a hexagonal arrangement for which we assign vessels as arterioles or venules in a pseudorandom fashion ('hex pseudorandom' in figure 8). In each group of 18 adjacent vessels, we randomly assign five to be venules and 13 to be arterioles. This strategy places each arteriole closer to a venule, on average, than the 'hex random' arrangement, making $\mathcal{R}_{art}$ typically lower in the 'hex random' or 'random random' arrangements.

To further explore the impact of vessel location and arteriole-to-venule spacing, we use the same vessel locations as in the primate data but assign vessels as arterioles or venules either randomly or psuedorandomly (assigning five of 18 vessels at a time). The random assignment of vessels (primate data random) has values of $\mathcal{R}_{art}$ similar to the 'random random' and 'hex random' arrangements. The pesudorandom assignment of vessels (primate data pseduorandom) has $\mathcal{R}_{art}$ typically smaller than the random cases, but larger than 'hex pseudorandom', suggesting that once the arterioles and venules are more uniformly arranged in a pseduorandom way, the more uniform vessel-to-vessel spacing in the hexagonal arrangement serves to reduce the resistance.

Next, to isolate the impact of non-uniform vessel spacing, we perturb each vessel location in the ideal primate configuration in a random direction. The perturbation distances are sampled from a normal distribution with a standard deviation selected so that, following perturbation, the ratio of the standard deviation to the average nearest neighbour vessel-to-vessel distance is the same as that in the *ex vivo* primate data. We label this distribution 'ideal perturbed' in figure 8. The $\mathcal{R}_{art}$ distribution shows very little variation from the $\mathcal{R}_{art}$ of the ideal arrangement, demonstrating that changing the vessel-to-vessel spacing slightly does not significantly affect the resistance. Of course, as the perturbation distance increases, $\mathcal{R}_{art}$ increases because the spacing between the arterioles and venules becomes less uniform. Adding very large perturbations to the *ex vivo* primate

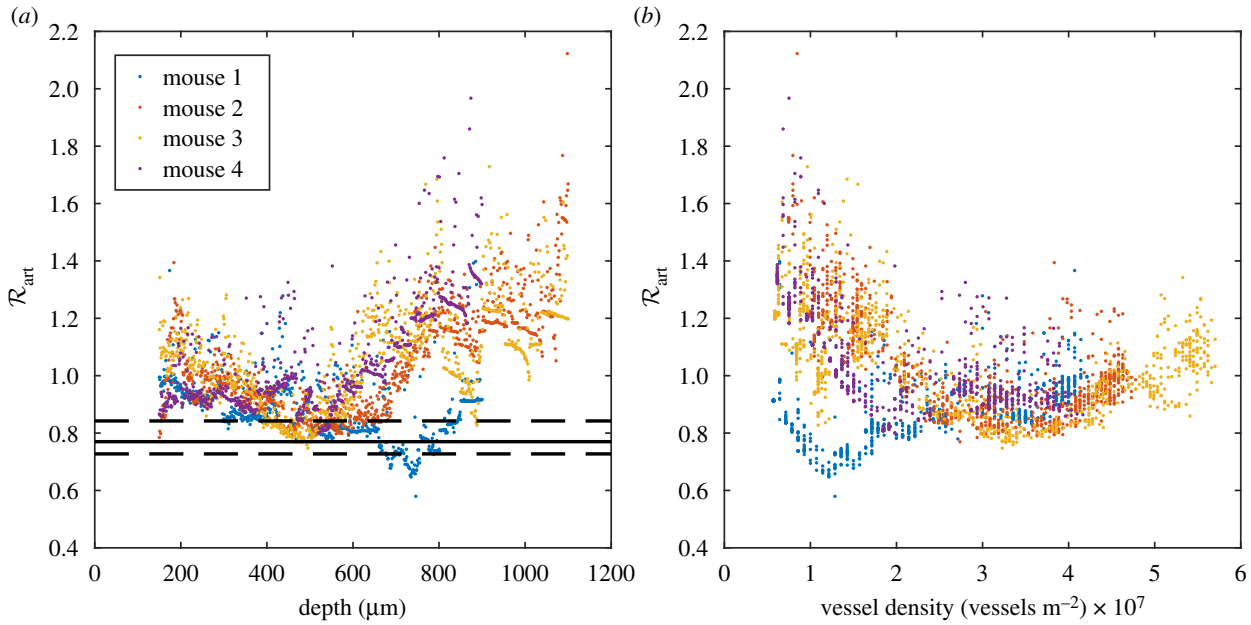

Figure 9. Dimensionless resistance $\mathcal{R}_{art}$ calculated based on vessel locations at various depths throughout the cortex from the four mice in figure 1 (*a*). The horizontal black lines indicate the resistance of the idealized arrangement, found at the average density (solid line) ± the standard deviation of the densities (dashed line) for all mice. $\mathcal{R}_{art}$ as a function of vessel resistance, showing that the variation in $\mathcal{R}_{art}$ with depth cannot be fully attributed to a change in vessel density (*b*).

arrangement produces an $\mathcal{R}_{art}$ distribution matching the 'random random' arrangement, as expected.

Other geometric arrangements produce similar distributions of $\mathcal{R}_{art}$. Square and triangular arrangements of vessels with the same vessel density ('square pseudorandom' and 'triangle pseudorandom') result in distributions similar to that for the hexagonal psuedorandom arrangement, again suggesting that the exact locations of the vessels are less important than having arterioles well mixed with venules. In summary, more uniform arrangements of arterioles and venules result in lower resistances, with pseudorandom assignment of vessels producing resistances lower than those of completely random assignments. The uniformity of the arteriole-to-venule spacing is more important than the uniformity of the vessel-to-vessel spacing.

3.7. Resistances in the mouse brain

To produce a statistical characterization of flow resistance in the mouse cortex, we calculate $\mathcal{R}_{art}$ using *ex vivo* vessel locations at many cross sections parallel to the cortical surface, spaced 1 μm apart in depth, from the four mice shown in figure 1. The dimensionless resistance $\mathcal{R}_{art}$ is shown in the left panel of figure 9 as a function of depth into the cortex. Also shown is the dimensionless resistance $\mathcal{R}_{art}$ for the idealized mouse arrangement calculated at the mean and ± 1 s.d. of the vessel density. The variation in $\mathcal{R}_{art}$ for the idealized arrangement owing to the difference in density is much less than the observed variation in $\mathcal{R}_{art}$ throughout the depth of the cortex, so density alone cannot explain the variation. Changing individual distances between arterioles and venules, and vessel ratio, account for most of the variation (see appendix A, figures 10 and 11). In the panel on the right in figure 9, we show $\mathcal{R}_{art}$ as a function of vessel density, further demonstrating that the variation in $\mathcal{R}_{art}$ throughout the cortex cannot be completely attributed to the change in vessel density.

The dimensionless resistance is typically lower in idealized arrangements than in arrangements based on *ex vivo* data. The few *ex vivo* cross sections with $\mathcal{R}_{art}$ lower than that in the idealized arrangement have higher density or a different vessel ratio. The median resistance for mouse 1 is closest to the resistance in the idealized arrangement because the median vessel ratio is closest to 1–3. (see appendix A)

The median values of $\mathcal{R}_{art}$ are 0.8469, 0.9817, 1.0482 and 0.9646 for mice 1, 2, 3 and 4, respectively. The median across all four mice is $\mathcal{R}_{art} = 0.9563$. The median resistance is considerably higher for the primate arrangement: $\mathcal{R}_{art} = 1.669$. The mouse resistances are lower because of the difference in the vessel ratio (as shown in figure 7) and the difference in density (as shown in figure 6).

4. Discussion

We begin this section with a brief summary. We calculate the hydraulic resistance of the parenchyma using the locations of penetrating arterioles and venules in the parenchyma for both mice and primates based on *ex vivo* data. Using approximately realistic vessel ratios (2–1 for primates and 1–3 for mice), we create idealized arrangements with equidistant spacing between all vessels and between arterioles and venules. When using regularly repeating patterns like the idealized arrangements, the dimensionless resistance, $\mathcal{R}_{art}$ converges to a constant as the domain size increases; this asymptotic behaviour illustrates the importance of calculating the resistance of an array of vessels, rather than the resistance among just a few vessels. The dimensionless resistance varies monotonically with vessel density: more densely packed arrays of vessels produce lower values of $\mathcal{R}_{art}$ which can be accurately estimated with a logarithmic curve. The vessel ratio impacts the dimensionless resistance; for example, from a dipole arrangement to an arrangement of two arterioles and one venule, or one arteriole and three

venules, $\mathcal{R}_{art}$ varies approximately 50%. The arrangement of arterioles and venules also affects the resistance; without changing vessel ratio or density, we vary the locations of the arterioles and venules, finding that less-ordered arrangements have higher resistance. Natural variations in the locations of arterioles and venules lead to a range of $\mathcal{R}_{art}$ in physiological data as well: we calculate $\mathcal{R}_{art}$ at various cross sections in mouse brains, showing the range of resistances owing to intra- and inter-animal variations.

Dimensionless resistances for mice are smaller than those for primates: $0.5 \leq R_{art} \leq 1.5$, compared to $R_{art} = 1.67$. The same trend occurs in idealized arrangements, where $\mathcal{R}_{art}$ differs by a factor of approximately 1.5. Species-specific models will be necessary for accuracy in future studies of flow in brain parenchyma. Qi *et al.* examine the impact of the vessel ratio on blood flow in the cerebral cortex, modelling the blood flow in the capillary bed as a porous medium. They find that an uneven ratio of vessels is important for blood perfusion and that the optimal ratio closely matches the ratios observed in multiple mammalian cortices [19].

Modelling parenchymal flow is challenging because of the uncertainty in the values of several parameters. The flow rate through the parenchyma is a quantity of considerable interest, but it remains largely unknown. The flow rate determines whether solutes are cleared primarily by diffusion or advection, which has implications for the development of Alzheimer's disease and drug delivery [8,9,11,20]. Another challenge is the uncertainty in the parenchymal permeability κ; published estimates differ by orders of magnitude [8,21], and permeability changes with brain state [22]. Pressure drops across brain tissue are largely unknown; only a single study has measured intracranial pressure simultaneously at more than one location [23]. Here we have focused on the mathematically tractable problem of the dimensionless resistance caused by the geometric arrangement of arterioles and venules, which links the unknown flow rates, permeabilities and pressure drops. We have provided values of the non-dimensional resistance $\mathcal{R}_{art}$: the dimensional resistance, R, scales linearly with κ and μ and can easily be calculated from $\mathcal{R}_{art}$. Determining the actual value of μ is straightforward, while obtaining a value for κ is not straightforward and controversial. When comparing mouse and primate brains in this work, we only describe the efficiency of the geometrical arrangement of the vessels, i.e. their ratios and spacings. It is possible that the brains of different species have different permeabilities, and the differences in permeability may be much more important for the dimensional resistance than the differences in geometrical arrangement we describe here.

Presently, the uncertainty associated with parenchymal permeability (estimates span several orders of magnitude) is much larger than the differences in $\mathcal{R}_{art}$ resulting from factors discussed in this work, including vessel ratio and the effects of convergence with array size, which change $\mathcal{R}_{art}$ by less than a factor of three. Before entering the extracellular space, fluid passes through gaps in astrocyte end feet that form the outer boundaries of the PVSs [6]. The size of these gaps is also largely unknown and their resistance may be dominant or have negligible effect [9,13,24]. However, as measurements of permeability and the size of endfoot gaps become more precise, it will become more important to calculate $\mathcal{R}_{art}$ accurately.

The importance of flow in the parenchyma is a matter of some debate as described in the recent review from Ray *et al.* [20] Despite using very different estimates for the parenchymal permeability κ, Jin *et al.* [12] and Holter *et al.* [8] both conclude that the resistance is so large that flow through the parenchyma is negligible and that diffusion, rather than convection, is the dominant mode of mass transport in the parenchyma. We show that accounting for the presence of multiple vessels may change their resistance estimates by a factor of three, but doing so is unlikely to change their main conclusions. However, Ray *et al.* estimate ISF velocities of 7–50 $\mu m\,min^{-1}$ [9]. Additionally, a recent network model of parenchymal flow estimated ISF velocities of 2–6 $\mu m\,min^{-1}$ [24]. Whether advection or diffusion dominates transport for these velocities depends on the size of the molecule in question, with the Péclet number quantifying the relative importance of these two modes of transport. However, even if advection is not as important as diffusion for mass transport in the parenchyma, advection is likely to dominate mass transport in PVSs, as described by Thomas [5], and because fluid exits PVSs via the parenchyma, parenchymal resistances will affect perivascular flows and are important to include in models of perivascular flows. Advection clearly plays a role in solute transport at some level since clearance from the whole brain by diffusion alone would produce a highly inhomogeneous distribution of solutes with very high concentrations near the centre of the brain.

The dimensionless resistance $\mathcal{R}_{art}$ can easily be incorporated into models of flow in the glymphatic system, such as the hydraulic network model developed by Tithof *et al.* [24] or other published models [10,25,26]. We provide three different ways to calculate $\mathcal{R}_{art}$. First, we give $\mathcal{R}_{art}$ in analytical form in equation (2.3). Second, $\mathcal{R}_{art}$ can be estimated as a function of vessel density for a given vessel ratio and arrangement using equation (3.1). Third, the dimensionless resistances calculated based on the vessel locations of *ex vivo* data and shown in figures 3 and 9 could be used directly.

Our model considers two-dimensional flow in planes perpendicular to an array of straight, parallel arterioles and venules. As seen in figure 1, these vessels are not completely straight and are not all parallel: a few even turn enough to run along the cross-sections. Also, we have assumed the parenchyma to be homogeneous and isotropic, while in reality it is penetrated by a network of capillaries. Qi *et al.* show that for blood flow, the network of capillaries can be approximated as a continuous, homogeneous porous medium [19], so assuming a homogeneous porous medium for the parenchyma may also be reasonable when considering perfusion of ISF at large scales. Each of these approximations affects the computed flow field and the hydraulic resistance.

Jin *et al.* [12] modelled transport of waste in the glymphatic system and found that increasing arteriolar density increases the mass transport. They also found that swapping the locations of the arterioles and venules decreased the mass transport. Although they considered both advective and diffusive mass transport, whereas our calculations of the hydraulic resistance relate only to advective mass transport, our conclusions are similar: increasing the density of the vessels decreases the resistance, which leads to increased advective mass transport.

We calculate $\mathcal{R}_{art}$ assuming that the volume flow rate exiting every arteriole is the same and the flow rate entering every venule is the same. This results in a different pressure at each arteriole and at each venule. The implications of this assumption could be explored in future work. An

alternative approach would be to specify the same pressure at each arteriole and at each venule and solve for the flow rates. This would require a straightforward numerical simulation. It is reasonable to suppose that physiological flows might fall somewhere between these two extremes. Which approach more closely resembles physiological flow will depend in part on the forces driving the flow; for example, if the flow is being driven by a steady global pressure gradient between the pial arterial PVSs and pial venous PVSs, and if most of the pressure drop occurs across the parenchyma, then specifying the same pressure for each vessel type might be more appropriate. Alternatively, if the flow is being driven by local pressure gradients generated by arteriole pulsations, specifying the same flow rate for each vessel type might be more appropriate. Flows driven by osmosis, functional hyperemia, poroelastic pumping or other mechanisms could each produce different distributions of flows and pressures among the various vessel boundaries. Which mechanisms are driving parenchymal flow is still an open question. Determining how the flows and resistances vary might give insight into the driving mechanisms, once experimental measurements of parenchymal flow become available.

Data accessibility. The original data for the locations of the mouse vasculature were collected by Blinder *et al.* [17,18] and are located at the following link. https://neurophysics.ucsd.edu/publications/AOH_Data.zip. The processed data are provided as the electronic supplementary material to this article as described in appendix A.

Authors' contributions. H.E.S.: data curation, formal analysis, visualization, writing—original draft; J.L. and J.H.T.: conceptualization, writing—review and editing; D.H.K.: conceptualization, funding acquisition, visualization, writing—review and editing; K.A.S.B.: conceptualization, data curation, writing—original draft, writing—review and editing. All authors gave final approval for publication and agree to be held accountable for the work performed therein.

Competing interests. The authors declare that they have no competing interests.

Funding. This work was supported by the NIH/National Institute on Aging (grant no. RF1AG057575) and by the US Army Research Office (grant no. MURI W911NF1910280).

Acknowledgements. We thank Pablo Blinder for helpful conversations and for providing data on the mouse brain.

Appendix A. Data for mouse and primate brains

A.1. Filtered penetrating vessel data for mice

The data from Blinder *et al.* [17,18] are provided as a series of points distributed along the centrelines of the vessels. Though penetrating venules and ascending veins are primarily oriented perpendicular to the cortical surface (along the *z*-direction), they occasionally deviate from that orientation and intersect a cross-section at a particular depth more than once. In those cases, we 'filter' the data by including only the midpoint of the intersections. Both the filtered and the unfiltered data are provided as the electronic supplementary material in the accompanying MATLAB file, 'Blinder_Coordinates.mat', where mouse 1, mouse 2, mouse 3 and mouse 4 are labelled 'au', 'co', 'db' and 'av', respectively. Each mouse has a set of coordinates for arterioles ('art') and venules ('ven') where columns 1, 2 and 3 correspond to X, Y and Z coordinates. The substructure 'originalstrands' contains the vessel strand index for each of the points in the coordinate set.

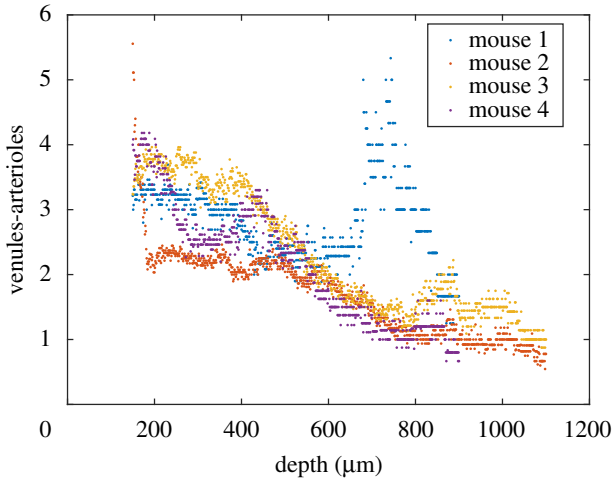

Figure 10. Venule–arteriole ratio for the four mice provided by Blinder *et al.* [17,18]. On average, mice have a ratio of approximately three venules to one arteriole, but these data show that the distribution of ratios can span a wide range, with mouse 2 having ratios ranging from 0.5 to 5.5, which generally decreases with depth.

Table 1. Vessel–vessel distances. (Mean ± standard deviation of the minimum distance between vessels for primates [16] and mice [17,18] (mice data have been filtered).)

	primates	mice
all vessels	181.82 ± 37.34 μm	103.51 ± 58.21 μm
arterioles to arterioles	206.52 ± 55.48 μm	212.45 ± 107.22 μm
venules to arterioles	185.00 ± 35.84 μm	158.01 ± 72.71 μm
arterioles to venules	229.34 ± 62.18 μm	128.10 ± 73.16 μm
venules to venules	332.96 ± 66.65 μm	118.95 ± 78.91 μm

A.2. Vessel–vessel distances for mice and primates

The distance between each vessel and its closest neighbour calculated from the vessel location data for the *in vitro* mouse and primate are provided in table 1.

A.3. Mouse vessel ratio

See figure 10.

A.4. Mouse vessel density

See figure 11.

Appendix B. Solution for the velocity and pressure fields

Slow incompressible viscous flow in a porous medium is governed by the continuity equation

$$\nabla \cdot \mathbf{u} = 0, \tag{B 1}$$

and Darcy's Law

$$\mathbf{u} = -\frac{\kappa}{\mu}\nabla p, \tag{B 2}$$

where $\mathbf{u} = [u(x, y), v(x, y)]$ is the superficial velocity (in Cartesian coordinates x, y), p is the pressure, κ is the permeability,

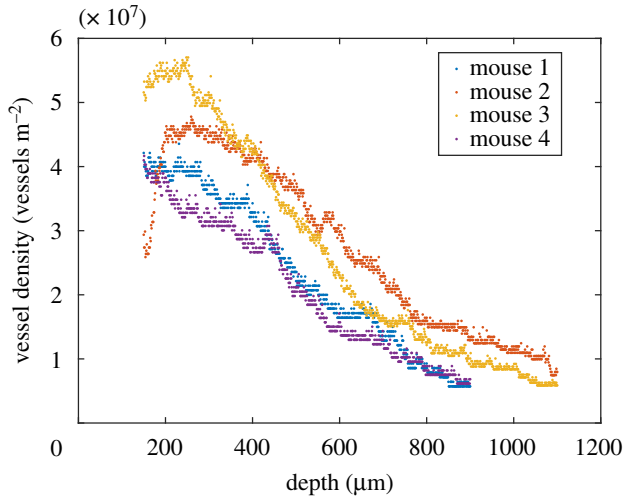

Figure 11. Vessel density for the four mice provided by Blinder *et al.* [17]. For all mice, the density decreases with depth, spanning a wide range of densities. This density (of all vessels) is approximately comparable to the approximately 1.5×10^7 penetrating arterioles m^{-2} that Adams *et al.* find in the mouse cortex [27]. They also find that the penetrating artery density is approximately uniform across cortical areas, with a slightly higher density in the visual cortex relative to the vibrissa.

and μ is the dynamic viscosity. If we assume that the permeability κ and the viscosity μ are uniform, then we can write Darcy's Law in the form

$$\mathbf{u} = \nabla\phi, \quad \phi \equiv -\frac{\kappa}{\mu}p, \tag{B 3}$$

where $\phi(x, y)$ serves as a velocity potential for the flow. Equation (B 1) then requires that ϕ satisfy Laplace's equation

$$\nabla^2\phi = 0. \tag{B 4}$$

Using the analogy with potential flow (of an inviscid fluid), we can introduce the stream function $\psi(x, y)$ such that

$$u = \frac{\partial\psi}{\partial y}, \quad v = -\frac{\partial\psi}{\partial x}, \quad \nabla^2\psi = 0, \tag{B 5}$$

and the complex potential

$$w(\zeta) = \phi(x, y) + \mathrm{i}\psi(x, y), \tag{B 6}$$

where $\zeta = x + \mathrm{i}y$, $\mathrm{i} = \sqrt{-1}$. For the boundary condition $u = v = 0$ at infinity, the complex velocity potential of a line source or sink is given by

$$w(\zeta) = \frac{q}{2\pi}\ln(\zeta), \tag{B 7}$$

where q is the volume flow rate per unit length, with $q > 0$ for a line source and $q < 0$ for a line sink. Laplace's equation is linear and homogeneous, so we can superimpose solutions and represent the flow owing to an array of $J = n_a + n_v$ arterioles and venules, at positions $\zeta_j = (x_j, y_j)$, by the complex potential

$$w(\zeta) = w(\zeta_0) + \sum_{j=1}^{J}\frac{q_j}{2\pi}\ln\left(\frac{\zeta - \zeta_j}{\zeta_0 - \zeta_j}\right), \tag{B 8}$$

where $w(\zeta_0)$ is an assigned value at some reference point $\zeta_0 = (x_0, y_0)$, subject to the condition that there be no net mass flux owing to the array,

$$\sum_{j=1}^{J} q_j = 0. \tag{B 9}$$

The corresponding expressions for the velocity potential, stream function, velocity components and pressure field are

$$\phi(x, y) = \phi(x_0, y_0) + \sum_{j=1}^{J}\frac{q_j}{4\pi}\ln\left(\frac{(x - x_j)^2 + (y - y_j)^2}{(x_0 - x_j)^2 + (y_0 - y_j)^2}\right), \tag{B 10}$$

$$\psi(x, y) = \psi(x_0, y_0) + \sum_{j=1}^{J}\frac{q_j}{2\pi}\left(\tan^{-1}\left(\frac{y - y_j}{x - x_j}\right) - \tan^{-1}\left(\frac{y_0 - y_j}{x_0 - x_j}\right)\right), \tag{B 11}$$

$$u(x, y) = \sum_{j=1}^{J}\frac{q_j}{2\pi}\left(\frac{x - x_j}{(x - x_j)^2 + (y - y_j)^2}\right), \tag{B 12}$$

$$v(x, y) = \sum_{j=1}^{J}\frac{q_j}{2\pi}\left(\frac{y - y_j}{(x - x_j)^2 + (y - y_j)^2}\right) \tag{B 13}$$

and

$$p(x, y) = p(x_0, y_0) - \frac{\mu}{\kappa}\sum_{j=1}^{J}\frac{q_j}{4\pi}\ln\left(\frac{(x - x_j)^2 + (y - y_j)^2}{(x_0 - x_j)^2 + (y_0 - y_j)^2}\right). \tag{B 14}$$

Streamlines of the flow are the family of curves $\psi(x, y) = \text{const}$.

Appendix C. Alternative boundary conditions

The solutions presented above are valid when pressure and velocity go to zero at infinity, but other boundary conditions can also be useful. We can instead consider a finite, rectangular domain of width w and height h, taking its boundaries either to be impenetrable or to be locations of zero pressure. Solutions for those two additional cases can readily be constructed via the method of images. For impenetrable boundaries, all sources and sinks are repeated and mirrored about the boundaries. For zero-pressure boundaries, *inverted* sources and sinks are repeated and mirrored about the boundaries. Thus, both solutions have complex potential

$$w(\zeta) = w(\zeta_0) + \sum_{m=-M}^{M}\sum_{n=-N}^{N}\sum_{j=1}^{J} b^m \cdot b^n \cdot \frac{q_j}{2\pi}\ln\left(\frac{\zeta - [nw + (-1)^n x_j + i(mh + (-1)^m y_j)]}{\zeta_0 - [nw + (-1)^n x_j + i(mh + (-1)^m y_j)]}\right), \tag{C 1}$$

where $b = 1$ for impenetrable boundaries and $b = -1$ for zero-pressure boundaries. The solution is exact when $M = N = \infty$; for finite M and N, larger values provide greater accuracy. When $b = 1$, the solution is identical to that provided by Ding & Wang [28]. When $b = -1$, the assignment of vessels as sources or sinks is flipped. The corresponding dimensionless resistance is

$$\mathcal{R}_{\text{art}} = \frac{n_a}{4\pi}\sum_{m=-M}^{M}\sum_{n=-N}^{N}\sum_{j=1}^{J} b^m \cdot b^n \times \left(\sum_{a=1}^{n_a}\frac{1}{n_a \cdot S_j}\ln\frac{[x_0-(nw+(-1)^n x_j)]^2+[y_0-(mh+(-1)^m y_j)]^2}{[x_a+r_{\text{art}}-(nw+(-1)^n x_j)]^2+[y_a-(mh+(-1)^m y_j)]^2} - \sum_{v=1}^{n_v}\frac{1}{n_v \cdot S_j}\ln\frac{[x_0-(nw+(-1)^n x_j)]^2+[y_0-(mh+(-1)^m y_j)]^2}{[x_v+r_{\text{ven}}-(nw+(-1)^n x_j)]^2+[y_v-(mh+(-1)^m y_j)]^2}\right). \quad (C\,2)$$

References

1. Plog BA, Nedergaard M. 2018 The glymphatic system in central nervous system health and disease: past, present, and future. *Annu. Rev. Pathol.* **13**, 379–394. (doi:10.1146/annurev-pathol-051217-111018)
2. Rasmussen MK, Mestre H, Nedergaard M. 2018 The glymphatic pathway in neurological disorders. *Lancet Neurol.* **17**, 1016–1024. (doi:10.1016/S1474-4422(18)30318-1)
3. Mestre H *et al.* 2018 Flow of cerebrospinal fluid is driven by arterial pulsations and is reduced in hypertension. *Nat. Commun.* **9**, 4878. (doi:10.1038/s41467-018-07318-3)
4. Mestre H *et al.* 2020 Cerebrospinal fluid influx drives acute ischemic tissue swelling. *Science (New York, NY)* **367**, eaax7171. (doi:10.1126/science.aax7171)
5. Thomas JH. 2019 Fluid dynamics of cerebrospinal fluid flow in perivascular spaces. *J. R. Soc. Interface* **16**, 20190572. (doi:10.1098/rsif.2019.0572)
6. Iliff JJ *et al.* 2012 A paravascular pathway facilitates CSF flow through the brain parenchyma and the clearance of interstitial solutes, including amyloid β. *Sci. Transl. Med.* **4**, 111–147. (doi:10.1126/scitranslmed.3003748)
7. Hannocks MJ, Pizzo ME, Huppert J, Deshpande T, Abbott NJ, Thorne RG, Sorokin L. 2018 Molecular characterization of perivascular drainage pathways in the murine brain. *J. Cereb. Blood Flow Metab.* **38**, 669–686. (doi:10.1177/0271678X17749689)
8. Holter KE *et al.* 2017 Interstitial solute transport in 3D reconstructed neuropil occurs by diffusion rather than bulk flow. *Proc. Natl Acad. Sci. USA* **114**, 9894. (doi:10.1073/pnas.1706942114)
9. Ray L, Iliff JJ, Heys JJ. 2019 Analysis of convective and diffusive transport in the brain interstitium. *Fluids and Barriers of the CNS* **16**, 6. (doi:10.1186/s12987-019-0126-9)
10. Vinje V, Eklund A, Mardal KA, Rognes ME, Støverud KH. 2020 Intracranial pressure elevation alters CSF clearance pathways. *Fluids Barriers CNS* **17**, 29. (doi:10.1186/s12987-020-00189-1)
11. Asgari M, de Zélicourt D, Kurtcuoglu V. 2016 Glymphatic solute transport does not require bulk flow. *Sci. Rep.* **6**, 38635. (doi:10.1038/srep38635)
12. Jin BJ, Smith AJ, Verkman AS. 2016 Spatial model of convective solute transport in brain extracellular space does not support a 'glymphatic' mechanism. *J. Gen. Physiol.* **148**, 489–501. (doi:10.1085/jgp.201611684)
13. Wang MX, Ray L, Tanaka KF, Iliff JJ, Heys J. 2021 Varying perivascular astroglial endfoot dimensions along the vascular tree maintain perivascular-interstitial flux through the cortical mantle. *Glia* **69**, 715–728. (doi:10.1002/glia.23923)
14. Romanò F, Suresh V, Galie PA, Grotberg JB. 2020 Peristaltic flow in the glymphatic system. *Sci. Rep.* **10**, 21065. (doi:10.1038/s41598-020-77787-4)
15. Ray LA, Pike M, Simon M, Iliff JJ, Heys JJ. Quantitative analysis of macroscopic solute transport in the murine brain. Preprint Research Square.
16. Adams DL, Piserchia V, Economides JR, Horton JC. 2015 Vascular supply of the cerebral cortex is specialized for cell layers but not columns. *Cereb. Cortex* **25**, 3673–3681. (doi:10.1093/cercor/bhu221)
17. Blinder P, Tsai PS, Kaufhold JP, Knutsen PM, Suhl H, Kleinfeld D. 2013 The cortical angiome: an interconnected vascular network with noncolumnar patterns of blood flow. *Nat. Neurosci.* **16**, 889–897. (doi:10.1038/nn.3426)
18. Blinder P, Tsai PS, Kaufhold JP, Knutsen PM, Suhl H, Kleinfeld D. 2013 Data used in The cortical angiome: an interconnected vascular network with noncolumnar patterns of blood flow. *Nat. Neurosci.* **16**, 889–897. (doi:10.1038/nn.3426)
19. Qi Y, Roper M. 2021 Control of low flow regions in the cortical vasculature determines optimal arterio-venous ratios. *Proc. Natl Acad. Sci. USA* **118**, e2021840118. (doi:10.1073/pnas.2021840118)
20. Ray LA, Heys JJ. 2019 Fluid flow and mass transport in brain tissue. *Fluids* **4**, 196. (doi:10.3390/fluids4040196)
21. Basser PJ. 1992 Interstitial pressure, volume, and flow during infusion into brain tissue. *Microvasc. Res.* **44**, 143–165. (doi:10.1016/0026-2862(92)90077-3)
22. Xie L *et al.* 2013 Sleep drives metabolite clearance from the adult brain. *Science (New York, NY)* **342**, 373–377. (doi:10.1126/science.1241224)
23. Eide PK, Holm S, Sorteberg W. 2012 Simultaneous monitoring of static and dynamic intracranial pressure parameters from two separate sensors in patients with cerebral bleeds: comparison of findings. *Biomed. Eng. Online* **11**, 66. (doi:10.1186/1475-925X-11-66)
24. Tithof J, Boster KAS, Bork PAR, Nedergaard M, Thomas JH, Kelley DH. Preprint. A network model of glymphatic flow under different experimentally-motivated parametric scenarios. *bioRxiv* 20210923461519.
25. Rey J, Sarntinoranont M. 2018 Pulsatile flow drivers in brain parenchyma and perivascular spaces: a resistance network model study. *Fluids Barriers CNS* **15**, 20. (doi:10.1186/s12987-018-0105-6)
26. Faghih MM, Sharp MK. 2018 Is bulk flow plausible in perivascular, paravascular and paravenous channels? *Fluids Barriers CNS* **15**, 17. (doi:10.1186/s12987-018-0103-8)
27. Adams MD, Winder AT, Blinder P, Drew PJ. 2018 The pial vasculature of the mouse develops according to a sensory-independent program. *Sci. Rep.* **8**, 9860. (doi:10.1038/s41598-018-27910-3)
28. Ding J, Wang S. 2018 Analytical solution for 2D inter-well porous flow in a rectangular reservoir. *Appl. Sci. (Switzerland)* **8**, 586. (doi:10.3390/app8040586)